Hierarchical Bayesian inference of saline permafrost constituents from electrical resistivity and temperature data

Xueyang Wang[1], Ming Xiao[2], Dmitry Nicolsky[3], Sergei Rybakov[4]

[1] Graduate student, Department of Civil and Environmental Engineering, The Pennsylvania State University, University Park, PA 16802, United States of America. Email: xxw5360@psu.edu.

[2] Professor, Department of Civil and Environmental Engineering, The Pennsylvania State University, University Park, PA 16802, United States of America. Email: mzx102@psu.edu.

[3] Assistant Professor, Geophysical Institute, University of Alaska Fairbanks, Fairbanks, AK 99775, United States of America. Email: djnicolsky@alaska.edu.

[4] Former Graduate student, Geophysical Institute, University of Alaska Fairbanks, Fairbanks, AK 99775, United States of America.

HIERARCHICAL BAYESIAN INFERENCE OF SALINE PERMAFROST CONSTITUENTS FROM ELECTRICAL RESISTIVITY AND TEMPERATURE DATA

XUEYANG WANG[1], MING XIAO[2], DMITRY NICOLSKY[3], AND SERGEI RYBAKOV[4]

Abstract. **Abstract:** Electrical resistivity tomography (ERT) provides high-resolution images of subsurface resistivity in permafrost, but quantitative interpretation in Arctic coastal settings is complicated by the coupled effects of ice content, pore-water salinity, pore connectivity, and surface conduction. This study develops a hierarchical Bayesian framework for probabilistic characterization of saline permafrost from ERT-derived resistivity and ground temperature data. The framework couples a soil freezing model with an electrical conduction model that represents pore solution and interfacial conduction and links temperature, salinity, specific surface area, unfrozen water saturation, and volumetric unfrozen water content to bulk resistivity. Compiled laboratory measurements, sparse site-specific observations, and prior geotechnical information are integrated to constrain petrophysical non-uniqueness. Parameter, observational, and model uncertainties are propagated to obtain posterior distributions of salinity, specific surface area, volumetric solid fraction, unfrozen water content, and ice fraction. Applications to flat-centered and low-centered polygon tundra near Utqiaġvik, Alaska, distinguish ice-rich permafrost from saline, partially unfrozen zones in broad agreement with borehole observations. The framework provides a transferable approach for uncertainty-quantified characterization of saline permafrost under limited site investigation data.

1. Introduction

Electrical and electromagnetic techniques have been widely used to investigate the spatial variability of active layers and shallow permafrost. Representative methods include electrical resistivity tomography (ERT) (Fortier et al. 2008, Hauck et al. 2011, Tourei et al. 2024) and electromagnetic (EM) methods (Minsley et al. 2012, Mikucki et al. 2015, Dafflon et al. 2016, Jones et al. 2023). These techniques provide spatially resolved measurements of subsurface electrical properties that are sensitive to variations in ground ice, unfrozen water content (UWC), salinity, and lithology. Mapping such variations is important for understanding biogeochemical processes and assessing future changes in natural and infrastructure environments in coastal Arctic communities (Shock and Boyd 2015, Hjort et al. 2022). However, permafrost constituents and thermal states cannot be uniquely determined from electrical measurements alone. Quantitative interpretation requires petrophysical relationships that link electrical responses to the physical, chemical, and thermal properties of frozen ground.

Key words and phrases. **Key words:** Hierarchical Bayesian inversion; electrical resistivity tomography; saline permafrost; petrophysical modeling; uncertainty quantification.

A quantitative link between geophysical measurements and permafrost properties requires an understanding of the mechanisms that control soil's electrical conductivity (EC), which is the inverse of electrical resistivity. Soil's EC mainly arises from electrolytic conduction through the bulk pore solution and mineral-water interfacial conduction (Rhoades et al. 1976, Revil et al. 1998, Friedman 2005, Glover 2016). Classical formulations, including Archie's law (Archie 1942), effective medium models (Maxwell and Niven 1881, Sen et al. 1981), and tortuosity models (Mualem and Friedman 1991), describe bulk conduction as a function of pore water conductivity, porosity, saturation, and pore network geometry. For medium- and fine-textured soils, charged clay minerals introduce an additional surface conduction pathway. The Waxman–Smits model extends Archie's law by adding a surface conductivity term to the EC model (Waxman and Smits 1968). Revil et al. (1998) further refined this framework by incorporating mineral surface properties, cation exchange capacity (CEC), counterion type, and pore water salinity, improving its applicability to clayey and saline soils.

Under frozen or partially frozen conditions, the electrical conductivity of soils is additionally governed by the ice-water phase transition and the redistribution of solute (Ostroumov et al. 2001). As temperature decreases, the progressive freezing of connected pore water reduces the continuity of liquid-phase conduction pathways (Ming et al. 2020, Gao et al. 2024). Solute exclusion during ice formation concentrates ions in the residual unfrozen water, increasing pore solution EC and depressing the freezing point (Zhou et al. 2020). At lower subzero temperatures, adsorbed water films may remain liquid after much of the connected pore water has frozen, shifting the dominant conductive pathway toward thin unfrozen water films and interfacial conduction along charged mineral surfaces (Chen et al., 2021; Jin et al., 2020). Thus, the electrical response of saline permafrost reflects the balance between pore solution and interfacial conduction, with salinity controlling pore solution conductivity and freezing behavior, and mineral surface properties controlling bound water retention and surface conduction (Anderson and Tice 1973, Rhoades et al. 1976, Revil et al. 1998, Jin et al. 2020). These coupled controls highlight the need for a quantitative model that links the electrical response of saline permafrost to pore solution and interfacial conduction while accounting for the effects of salinity and mineral surface properties on unfrozen water retention and soil freezing characteristics.

At the field scale, EC-based petrophysical relationships can be embedded within geophysical inversion frameworks to estimate the spatial distribution of permafrost constituents. A typical approach is the four-phase model (4PM), which combines seismic and electrical measurements to compute air, ice, liquid water, and solid phase fractions (Hauck et al. 2011, Rossi et al. 2022). The 4PM has been successfully applied to permafrost in mountainous regions. However, its application to Arctic sedimentary permafrost faces challenges. In coastal or organic-rich

environments, spatially varying salinity, mineral composition, and organic matter can depress the freezing point, altering the geophysical thresholds (e.g., EC) used to distinguish frozen from unfrozen ground (Angelopoulos et al. 2021). The validation of 4PM in alpine environments, which often consist of rock, raises concerns about its suitability for sediment-based permafrost. Dafflon et al. (2016) proposed an alternative framework to combine electrical measurements and ground thermal data for the inversion of permafrost properties. The framework was tailored to the Arctic Coastal Plain, but its reliance on site-specific empirical relationships limits its transferability. Local variations in drainage, microtopography, and biogeochemistry can modify subsurface properties and invalidate best-fit parameters derived from a specific site (Shur et al. 2005).

The transferability of empirical petrophysical parameters is further constrained by data limitations and procedural biases during model calibration. Geophysical inversion routines can introduce artifacts through regularization or data smoothing (Wagner et al. 2019). Ground temperature measurements provide valuable constraints, but sensors are often sparse, and interpolating two-dimensional thermal profiles from sparse point measurements can lead to significant misinterpretation. Borehole data also typically have much lower spatial resolution than dense, centimeter-scale electrical resistivity profiles. This mismatch between sparse ground-truth observations and high-resolution geophysical data makes robust calibration and validation of permafrost petrophysical models especially challenging.

To address the calibration and transferability challenges, a framework is needed that can accommodate sparse ground-truth observations while explicitly accounting for uncertainty in both measurements and petrophysical relationships. Bayesian inference provides such a framework. By representing model parameters as probability distributions that are updated through Bayes' theorem (Puga et al. 2015), Bayesian methods enable the uncertainty of geophysical inversion, ground temperature measurements, laboratory experiments, and prior geotechnical information to propagate consistently into estimates of permafrost properties. Hierarchical Bayesian models are particularly useful for permafrost applications because they allow parameters to share information across datasets while retaining site-specific variability, improving parameter estimation under sparse observations and reducing overfitting (Gelman et al. 2013). Accordingly, hierarchical Bayesian modeling (HBM) has been widely applied in geotechnical and geophysical studies to characterize systems with substantial spatial variability and to quantify uncertainty in model predictions (Yang et al. 2015, Bozorgzadeh et al. 2019, Mavritsakis et al. 2022).

In this study, we developed and calibrated a semi-empirical petrophysical model that links EC to soil freezing characteristics of saline permafrost. The model explicitly relates five key permafrost

attributes (volumetric unfrozen water content θ_{uw}, volumetric ice content θ_i, volumetric soil solid content θ_s, specific surface area S_a, and salinity s_0) to the bulk electrical response of frozen soils through pore solution conduction and surface conduction. Laboratory EC and UWC measurements from published literature were used to constrain global model parameters for saline frozen soils. We then integrated the governing equations into a hierarchical Bayesian inversion framework to provide probabilistic interpretations of the five permafrost attributes from ERT and ground temperature data.

In this paper, the governing equations for interpreting θ_{uw}, θ_i, θ_s, s_0, and S_a in saline permafrost are established in Section 2. Section 3 formulates the hierarchical Bayesian inverse problem and describes how laboratory data, prior geotechnical information, site-specific ground temperature profiles, and ERT-inverted resistivity profiles are integrated to estimate posterior distributions of permafrost attributes while propagating observational, parameter, and model uncertainties. Section 4 calibrates the proposed method using laboratory experiments. Section 5 applies the framework to a coastal tundra site in Utqiaġvik, Alaska, using data from two geophysical field campaigns.

2. Petrophysical model for saline permafrost

This section presents the theoretical formulation and derivation of the proposed petrophysical model for inferring saline permafrost attributes θ_{uw}, θ_i, θ_s, s_0, and S_a under partially frozen conditions. The model consists of two coupled components. The first component is an EC model developed from the formulation of Revil et al. (1998), which represents the bulk electrical response of frozen saline soils as the combined contribution of pore solution conduction and surface conduction along charged mineral surfaces. The second component is a simplified UWC model, based on Jin et al. (2020), which describes the effects of temperature, salinity, and specific surface area on ice-water partitioning in soil pores. The two components are coupled through the common variables T, s_0, and S_a, with the UWC model providing θ_{uw} to the electrical conduction calculation. Specifically, s_0 controls freezing point depression and pore solution conductivity, whereas S_a influences unfrozen-water retention and interfacial surface conduction. Here, θ_{uw}, θ_i, and θ_s are volumetric fractions [m^3 m^{-3}], s_0 is the initial pore water salinity [mol L^{-1}], and S_a is the specific surface area [m^2 g^{-1}].

2.1. Electrical conductivity model

For a clean unfrozen porous medium in which electrical current is carried only by the connected pore solution, Archie's law (Archie 1942, Winsauer et al. 1952) can be written as

$$\sigma = \frac{\sigma_f}{F} \tag{1}$$

$$F = \phi^{-m} S_w^{-n} \tag{2}$$

where σ is the bulk conductivity of soil [S m^{-1}], σ_f is the pore solution conductivity of the pore water [S m^{-1}], and F is the formation factor determined by porosity ϕ, water saturation S_w, cementation exponent m, and saturation exponent n.

The classical Waxman-Smits model (Waxman and Smits 1968) extends Archie's law for clayey porous media by adding a surface conduction term associated with exchangeable cations:

$$\sigma = \frac{1}{F}\left(\sigma_f \ + BQ_v\right) \tag{3}$$

where B is the equivalent surface conductance of exchangeable cations, and Q_v is the cation exchange capacity per unit pore volume.

Revil et al. (1998) developed a physically based extension of the Waxman–Smits dual-conduction framework by separating cationic and anionic current contributions and accounting for interfacial counterion conduction at the mineral-water interface:

$$\begin{aligned}\sigma = \frac{\sigma_f}{F^*}\Big[1 - t^+ + F^*\xi \\ + \frac{1}{2}\left(t^+ - \xi\right)\left\{1 - \frac{\xi}{t^+} + \sqrt{\left(1 - \frac{\xi}{t^+}\right)^2 + \frac{4F^*\xi}{t^+}}\right\}\Big]\end{aligned} \tag{4}$$

where ξ represents the ratio between interfacial surface conduction and pore-fluid conduction, F^* is the effective formation factor corrected for partial unfrozen saturation, and t^+ is the Hittorf transport number of the cation in free electrolyte. In this study, the auxiliary variables in Eq. (4) are parameterized as

$$\xi = \frac{K_s S_a}{\sigma_f} \tag{5}$$

$$\frac{1}{F^*} = \phi^m S_{ru}^n \tag{6}$$

$$\sigma_f = \frac{a_s s_0}{S_{ru}} \times 10^3 \tag{7}$$

where K_s is the effective surface conduction coefficient [S g m^{-3}], lumping the surface charge density, counterion mobility, mineralogy, and electrical double layer effects; σ_f is a function of salinity s_0 and liquid water saturation $S_{ru} = \theta_{uw}/\phi = \theta_{uw}/(1-\theta_s)$; and a_s is a fluid conductivity coefficient [S m^2 mol^{-1}]. The derivation of Eqs. (5)–(7) is provided in **Appendix A**.

2.2. UWC model

For the UWC model, we attribute the persistence of unfrozen water at subzero temperatures to three mechanisms: freezing-point depression caused by dissolved salts in bulk pore water, interfacial effects in capillary and weakly bound water, and adsorption forces in strongly bound water (Bublik et al. 2023, Dou et al. 2016, Jin et al. 2020, Wang & Hu 2023). The microscale UWC model of Jin et al. (2020) serves as the foundation for the UWC formulation because it explicitly represents the combined effects of dissolved salts, interfacial water, and adsorption forces on unfrozen water retention during freezing. The model adopts a parsimonious formulation in which S_a scales the capacity for interfacial and adsorbed water retention, whereas s_0 controls freezing point depression and thereby modifies the temperature dependence of UWC:

$$w_u = S_a^{\ell}\sqrt{273+T}\left[\left(\left(\alpha_0+\alpha_1 s_0\right)|T|^{-0.5}+\alpha_2 s_0\right)\right]+0.05S_a, T \le T_{fp} \tag{8}$$

where w_u is the gravimetric unfrozen water content; ℓ is an empirical coefficient estimated in this study and was set to 0.5 based on the linear regression and optimization results shown in **Figure S1**. T_{fp} is the freezing point, above which all pore water is assumed to remain unfrozen. The derivation and simplification of Eq. (8) are provided in **Appendix B**.

The expression of T_{fp} is given as a function of s_0 (Banin and Anderson 1974, Amankwah et al. 2021):

$$T_{\mathrm{fp}} = -\frac{RT_0^2}{L_f b}s_0 \approx K_{\mathrm{fp}}s_0 \tag{9}$$

where the freezing point of pure water $T_0 = 273.15$ [K]; the gas constant $R = 8.314$ [J mol^{-1} K^{-1}]; the latent heat of fusion $L_f = 6010$ [J mol^{-1}]; the coefficient $b = 10^3/(M_w \bullet n_m)$; the molecular weight of water $M_w = 18$ [g mol^{-1}]; n_m is the number of ions produced when the dissolved salt dissociates; and the unit of s_0 is mol/L. K_{fp} [°C mol^{-1} L] is the freezing point depression coefficient defined by Eq. (9). Assuming ideal dissociation, $n_m = 2$ for NaCl and KCl and $n_m = 3$ for Na_2SO_4 and $CaCl_2$, giving $K_{fp} \approx -3.72$ and -5.57 °C $(mol\,L^{-1})^{-1}$, respectively. Thus, for NaCl, a 1 $mol\,L^{-1}$ increase in s_0 corresponds to an approximately 3.72 °C decrease in the freezing point.

2.3. Governing equations of petrophysical model

To interpolate spatial patterns in permafrost, the subsurface profile is discretized into a finite number of soil elements. Each element is represented by volumetric fractions of mineral solids θ_s, air θ_a, unfrozen water θ_{uw}, and ice θ_i, which satisfy

$$\theta_s + \theta_a + \theta_{uw} + \theta_i = 1 \tag{10}$$

In the electrical model, mineral grains, air, and ice are treated as non-conductive bulk phases. Electrical current is assumed to be carried only by the connected unfrozen pore brine and by surface conduction along the mineral-water interface.

The modeled electrical resistivity $\mathcal{R}$ [Ω m] is obtained as the reciprocal of the bulk electrical conductivity σ calculated from Eq. (4):

$$\mathcal{R} = \frac{1}{\sigma} \tag{11}$$

For $T < T_{fp}$, the gravimetric unfrozen water content w_u is calculated from Eq. (8), and the volumetric unfrozen water content is related to w_u by

$$\theta_{uw} = G_s \theta_s w_u, \quad T < T_{fp} \tag{12}$$

where G_s is the specific gravity of soil grains.

At $T \geq T_{fp}$, all water within the non-air pore volume is assumed to be unfrozen,

$$\theta_{uw} = G_s \theta_s \quad w_u|_{T=T_{fp}} = 1 - \theta_s - \theta_a, \quad T \geq T_{fp} \tag{13}$$

Solving Eq. (13) for θ_s gives

$$\theta_s = \frac{1 - \theta_a}{1 + G_s \quad w_u|_{T=T_{fp}}} \tag{14}$$

2.4. Determination of inverse problem formulation

Combining the governing relationships in Eqs. (4)-(14) the permafrost attributes model defines a forward mapping from six permafrost attributes (θ_{uw}, θ_i, θ_s, θ_a, s_0, and S_a) and thermal state T to soil electrical responses $\mathcal{R}$.

For a prescribed temperature T, the forward calculation uses θ_a, s_0, and S_a as inputs. The freezing point temperature T_{fp} is first calculated from Eq. (9). The θ_s is then determined from

the fully unfrozen boundary condition in Eqs. (13) and (14). For $T < T_{fp}$, the gravimetric unfrozen water content w_u is evaluated at the prescribed temperature using Eq. (8), and θ_{uw} is calculated from Eq. (12). The ice fraction θ_i is obtained from the phase-volume relationship in Eq. (10), and the electrical resistivity $\mathcal{R}$ is calculated from Eq. (11) and the electrical conductivity model in Eqs. (4)-(7).

In the inverse formulation, the air fraction θ_a is assumed to be negligible under near-saturated permafrost conditions or is specified from prior information when partial saturation is expected. For prescribed T and specified θ_a, s_0 and S_a are the two independent unknowns. The governing equation system maps each candidate s_0 and S_a to a unique resistivity $\mathcal{R}$. Because the inversion provides only one resistivity constraint at each depth, the problem retains one effective degree of freedom and is therefore underdetermined.

The hierarchical Bayesian framework regularizes this underdetermined problem by combining the resistivity likelihood with prior information and physical admissibility constraints over the permafrost attributes. Prior distributions constrain the plausible ranges of the directly inferred variables s_0 and S_a, while the derived attributes θ_s, θ_{uw}, and θ_i are evaluated against their prescribed prior supports. Laboratory calibrated distributions constrain the UWC and EC model parameters, and site-specific geotechnical priors or borehole conditioning further restrict the admissible attribute space. The Bayesian formulation therefore confines the inversion to physically and geotechnically plausible regions of the solution space and expresses the remaining ambiguity through posterior uncertainty and parameter correlations. In laboratory calibration, $\mathcal{R}_{pred}$ is compared with $\mathcal{R}_{lab}$, and in field applications it is compared with the ERT-inverted profile $\mathcal{R}_{pf}$. The complete forward and inverse workflow are summarized in Figure 1.

3. Bayesian formulation of the inverse problem

3.1. Hierarchical Bayesian workflow

For concise notation, the unknown permafrost attributes in inversion formulation are collected in the vector $\mathbf{A} = [\mathbf{s_0}, \boldsymbol{\theta}_\mathbf{uw}, \boldsymbol{\theta}_\mathbf{i}, \boldsymbol{\theta}_\mathbf{s}, \mathbf{S_a}]$. The air fraction θ_a is prescribed empirically based on the expected saturation state and is not treated as an inferred variable, thereby reducing the dimensionality of the inverse problem. The three EC model parameters in Eqs. (4)-(6) and three UWC model parameters in Eq. (8) are collected in $\boldsymbol{\alpha} = [\boldsymbol{\alpha_0}, \boldsymbol{\alpha_1}, \boldsymbol{\alpha_2}, \mathbf{m}, \mathbf{n}, \mathbf{K_s}]$. The datasets are distinguished according to their roles in the hierarchical workflow. The compiled laboratory database is denoted by $\mathbf{D_{lab}} = [\mathcal{R}_\mathbf{lab}, \mathbf{T_{lab}}, \mathbf{A_{lab}}]$, where $\mathcal{R}_\mathbf{lab}$, $\mathbf{T_{lab}}$, and $\mathbf{A_{lab}}$ contain laboratory resistivity, temperature, and soil property measurements, respectively. Site-specific borehole data are denoted by $\mathbf{D_{bh}} = [\mathcal{R}_\mathbf{bh}, \mathbf{T_{bh}}, \mathbf{A_{bh}}]$, where borehole measurements are used to update site-specific model parameters or define informative attribute priors. The

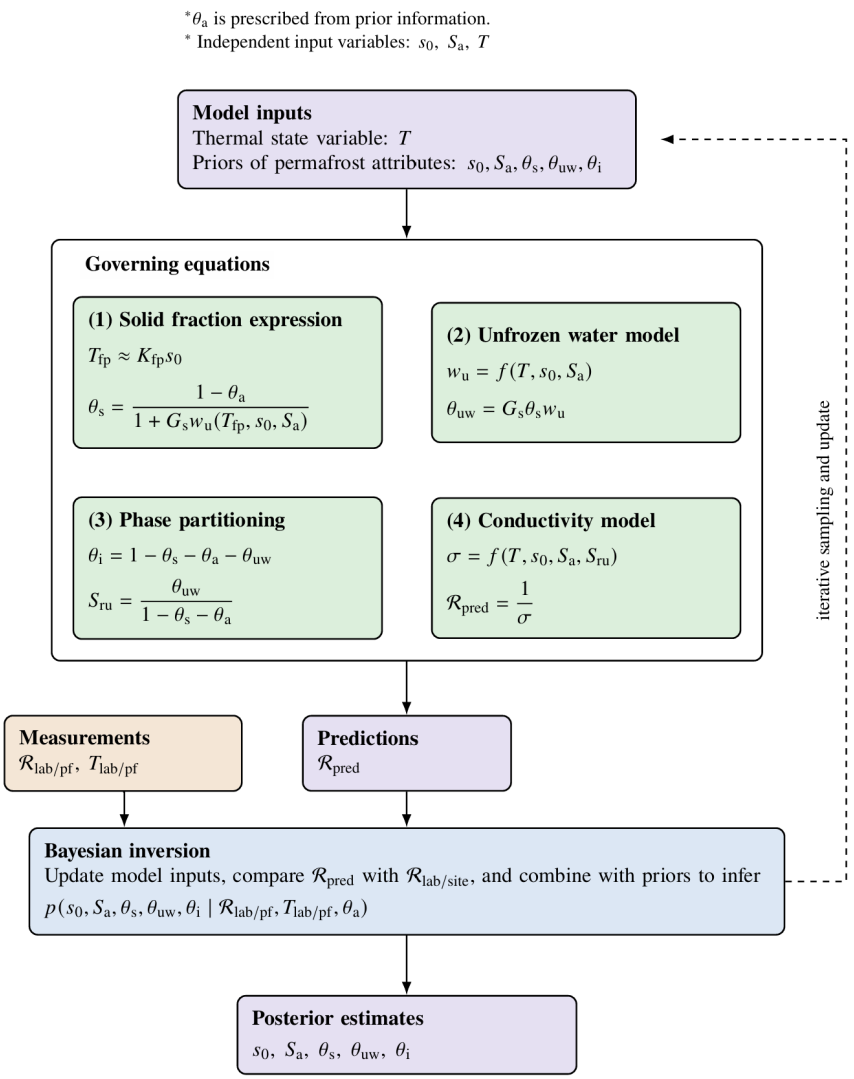


FIGURE 1. Schematic framework of the permafrost attributes model and Bayesian inversion.

continuous field profiles used for inversion are denoted by $\mathbf{D_{pf}} = [\mathcal{R}_{\mathbf{pf}}, \mathbf{T_{pf}}]$. The predicted electrical resistivity $\mathcal{R}_{\text{pred}}$ is computed through the forward operator $\mathbf{G}$, which implements the governing equations in **Section 2**.

$$\mathcal{R}_{\text{pred}} = \mathbf{G}(\mathbf{A}, \boldsymbol{\alpha}, \boldsymbol{T}) \tag{15}$$

The workflow is summarized in Figure 2. Previous literature informed priors $p_0(\boldsymbol{\alpha})$ on the model parameters are first updated using $\mathbf{D_{lab}}$, yielding the laboratory calibrated parameter distribution $p_{lab}(\boldsymbol{\alpha})$. Borehole observations near study site are then used to update this distribution and obtain the site-specific model parameter distribution $p_{site}(\boldsymbol{\alpha})$. This distribution serves as the model parameter prior in the subsequent field-profile inversions. The field data $\mathbf{D_{pf}}$ are then used to estimate posterior distributions of the inferred permafrost attributes $p_{\text{inf}}(\mathbf{A})$.

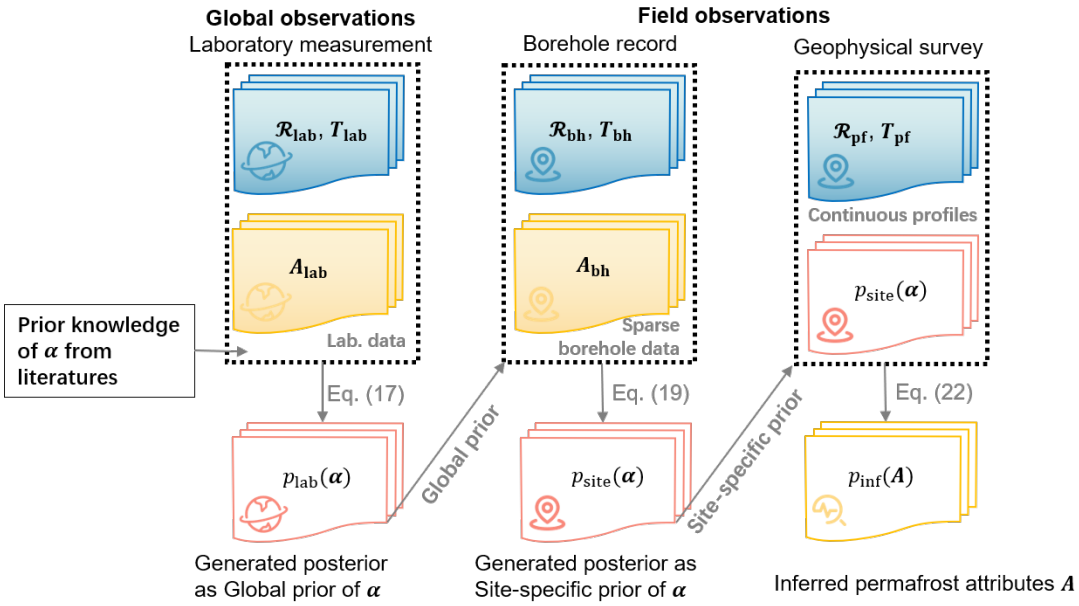


FIGURE 2. Hierarchical workflow for laboratory calibration, site-specific conditioning, and profile-scale inversion of permafrost attributes. The literature-informed model parameter distribution is first updated using the compiled laboratory database. Site-specific borehole and geophysical observations are then used to update model parameters or define informative attribute priors. These distributions are combined with continuous resistivity and temperature profiles to estimate posterior distributions of permafrost attributes.

3.2. Hierarchical calibration of model parameters

Hierarchical Bayesian modeling is used to estimate the UWC and EC model parameters $\boldsymbol{\alpha}$ from compiled laboratory datasets $\mathbf{D}_{lab}$. To represent variability among soil types and experimental conditions, the parameter vector for laboratory group c is written as

$$\boldsymbol{\alpha}_c = \boldsymbol{\alpha}_{\mathbf{m}} + \boldsymbol{\alpha}_{\mathbf{d},c} \tag{16}$$

where $\boldsymbol{\alpha}_{\mathbf{m}}$ is the mean parameter vector shared across all laboratory groups, and $\boldsymbol{\alpha}_{\mathbf{d},c}$ is the deviation of group c from this mean.

Let $\mathbf{D}_{lab}^{c}$ denote the observations for laboratory group c. The laboratory calibration is represented by

$$p\left(\boldsymbol{\alpha}_{\mathbf{m}}, \{\boldsymbol{\alpha}_{\mathbf{d},c}\}_{c=1}^{C} \mid \mathbf{D_{lab}}\right) \propto \left[\prod_{c=1}^{C} p\left(\mathbf{D}_{lab}^{c} \mid \boldsymbol{\alpha}_{\mathbf{m}} + \boldsymbol{\alpha}_{\mathbf{d},c}\right) p\left(\boldsymbol{\alpha}_{\mathbf{d},c}\right)\right] p\left(\boldsymbol{\alpha}_{\mathbf{m}}\right) \tag{17}$$

where C is the number of laboratory groups and the likelihood function $p\left[\mathbf{D}_{\mathbf{lab}}^{c} \mid \boldsymbol{\alpha}_{\mathbf{m}} + \boldsymbol{\alpha}_{\mathbf{d},c}\right]$ evaluates the agreement between the observations and model predictions for each laboratory group. The hierarchical structure allows individual groups to deviate from the global mean while sharing information across the compiled database.

The resulting laboratory-calibrated parameter distribution is denoted by

$$p_{lab}(\boldsymbol{\alpha}) \equiv p\left(\boldsymbol{\alpha}_{\mathbf{m}} \mid \mathbf{D_{lab}}\right) \tag{18}$$

For the subsequent site-specific update, $\boldsymbol{\alpha}_{\mathbf{m}}$ is held fixed at the laboratory-calibrated value, and the borehole observations are used to estimate the site-specific deviation $\boldsymbol{\alpha}_{\mathbf{d},site}$. The resulting site-conditioned parameter distribution is

$$\begin{aligned} p_{site}(\boldsymbol{\alpha}) &\equiv p\ \left(\boldsymbol{\alpha}_{\mathbf{d},site} \mid \mathbf{D_{bh}}, \mathbf{D_{lab}}\right) \\ &\propto p\left(\mathbf{D_{bh}} \mid \boldsymbol{\alpha}_{\mathbf{m}} + \boldsymbol{\alpha}_{\mathbf{d},site}\right) p_{lab}\left(\boldsymbol{\alpha}_{\mathbf{m}} + \boldsymbol{\alpha}_{\mathbf{d},site}\right) \end{aligned} \tag{19}$$

3.3. Prior distribution of inferred permafrost attributes

The prior distribution $p_0(\mathbf{A})$ constrains the permafrost attributes to physically plausible ranges and thereby regularizes the underdetermined inverse problem. Depending on the amount and reliability of available information, the prior distributions are specified as non-informative, weakly informative, or strongly informative.

A non-informative prior is represented by a uniform distribution over its physical bounds:

$$\mathbf{A}_j \sim\ \mathrm{U}(\mathbf{A}_{j,\min},\ \mathbf{A}_{j,\max}) \tag{20}$$

where j indexes the different permafrost attributes, and $A_{j,\min}$ and $A_{j,\max}$ are the lower and upper admissible bounds of attribute A_j. For example, the volumetric fractions θ_{uw}, θ_i, and θ_s are bounded between 0 and 1.

When approximate information is available, a weakly informative prior is used to guide the inversion toward plausible values without imposing a narrow constraint. This type of prior is useful when estimates are available from general site knowledge, literature, or previous surveys but remain uncertain. A broad normal distribution can be used for this purpose:

$$\mathbf{A}_j \sim \text{Normal}(\mu_j, \tau_j^2) \tag{21}$$

where μ_j is a physically plausible estimate of the attribute and τ_j^2 specifies a broad prior variance that reflects uncertainty of the available information. For example, an ice-rich permafrost layer may be assigned a relatively lower prior mean for θ_s, while τ_j^2 is chosen so that the prior distribution spans the plausible range of soil grain fraction reported for similar permafrost conditions.

When direct measurements are available, a strongly informative prior can be specified using the same normal form as Eq. (21). At borehole locations, μ_j is set to the measured value of attribute A_j, and τ_j^2 is assigned a small value that reflects the expected measurement uncertainty. These strongly informative priors provide local constraints on selected permafrost attributes and can be applied only where reliable borehole measurements are available.

3.4. Uncertainty models for geophysical and thermal observations

Uncertainty in the ERT-inverted resistivity profiles was represented in log-resistivity space. When the Jacobian matrix from the ERT inversion was available, the cell-wise resistivity uncertainty was estimated from an approximate model covariance matrix that accounts for data errors and inversion regularization. When the Jacobian matrix was unavailable or computationally impractical to obtain, a depth-dependent uncertainty model was used to represent the progressive loss of ERT sensitivity and spatial resolution with depth. This treatment accounts for uncertainty arising from the nonuniqueness and regularization of the ERT inverse problem, as well as measurement and electrode-contact errors (Alsharari et al. 2020, Khabaz et al. 2024). The detailed formulations used to quantify geophysical and thermal uncertainties are provided in **Text S1** of the **Supporting Information**.

Uncertainty in the reconstructed ground-temperature profiles was quantified using the posterior predictive distribution of the process-based Bayesian thermal model developed by Groenke et al. (2023). The model reconstructs continuous temperature profiles from sparse borehole measurements and long-term meteorological forcing from ERA5-Land (Muñoz-Sabater et al. 2021). It represents 1D heat conduction, surface forcing, geothermal heat flux, snow insulation, and latent-heat effects associated with soil freezing following Dall'Amico et al. (2011). The

resulting depth-specific posterior means and standard deviations were used to represent $\mathbf{T}_{pf}$ and its uncertainty in the field inversions.

3.5. Inference of permafrost attributes from site-specific observations

Bayesian inference estimates the joint posterior distribution of the permafrost attributes and model parameters by combining site-specific observations with prior information. The posterior distribution is expressed as

$$p\left(\mathbf{A},\boldsymbol{\alpha} \mid \mathbf{D_{pf}}, \mathbf{D_{bh}}\ \right) \propto p\left(\mathcal{R}_{\mathbf{pf}} \mid \mathbf{A}, \boldsymbol{\alpha}, \mathbf{T_{pf}}\right)\ p_0(\mathbf{A}) p_{site}(\boldsymbol{\alpha}) \tag{22}$$

The likelihood $p\left(\mathcal{R}_{\mathbf{pf}} \mid \mathbf{A}, \boldsymbol{\alpha}, \mathbf{T_{pf}}\right)$ evaluates the agreement between the ERT-inverted resistivity profile and the corresponding forward model prediction. The residuals are modeled in log-resistivity space and the corresponding log-likelihood is

$$\begin{aligned} &\log p\left(\mathcal{R}_{\mathbf{pf}} \mid \mathbf{A}, \boldsymbol{\alpha}, \mathbf{T_{pf}}\right) \\ &\qquad = -\frac{1}{2} \sum_{i=1}^{d} \left[\frac{\left(\ln \mathcal{R}_{pf,i} - \ln \mathcal{R}_{pred,i}\right)^2}{\tau^2_{\ln \mathcal{R},i}} + \ln\left(2\pi \tau^2_{\ln \mathcal{R},i}\right) \right] \end{aligned} \tag{23}$$

where d is the number of resistivity values in the extracted profile; and $\tau^2_{\ln \mathcal{R},i}$ is the cell-wise residual variance in log-resistivity space, incorporating the petrophysical model discrepancy, uncertainty of the ERT-inverted resistivity, and uncertainty propagated from $\mathbf{T}_{pf}$ through the forward model.

4. Laboratory calibration and global parameter distribution

This section presents the global calibration results obtained from $\mathbf{D_{lab}}$ and evaluates the performance of the proposed coupled petrophysical model. Details of the compilation of the laboratory database $\mathbf{D_{lab}}$ are provided in **Text S2 of the Supporting Information**. Following the hierarchical formulation in Eqs. (16)–(17), the laboratory UWC and EC measurements are used to estimate the posterior distributions of the global mean parameters $\boldsymbol{\alpha}_{\mathbf{m}}$ and the group-specific deviations $\boldsymbol{\alpha}_{\mathbf{d},c}$. Posterior predictions are then compared with laboratory observations across soil types, temperatures, and salinity conditions to assess whether the model reproduces the observed soil freezing and electrical responses. The resulting distribution $p(\boldsymbol{\alpha}_{\mathbf{m}} \mid \mathbf{D_{lab}})$ is subsequently used as the prior $p_{lab}(\boldsymbol{\alpha})$ for the site-specific parameter calibration.

4.1. Model performance and posterior distribution

The model predictions are compared with laboratory observations for eight sample groups (Liu et al., 2020; Luo et al., 2024; Pandit & King, 1979; Tang et al., 2020), including sandstone, limestone,

quartz sand, sand, clayey silt, lean clay, and red clay (Figure 3). Posterior-median predictions yielded RMSE values of 4.75 % for θ_{uw} and 0.169 for $\log_{10}\mathcal{R}$ across the observations in $\mathbf{D_{lab}}$, with 95% posterior predictive coverage of 96.5% and 98.2%, respectively. The model captures the main temperature-dependent trends, with θ_{uw} generally increasing and $\mathcal{R}$ decreasing as temperature approaches the freezing point. The predictions also reproduce the salinity dependence, with higher s_0 corresponding to higher θ_{uw} and lower $\mathcal{R}$.

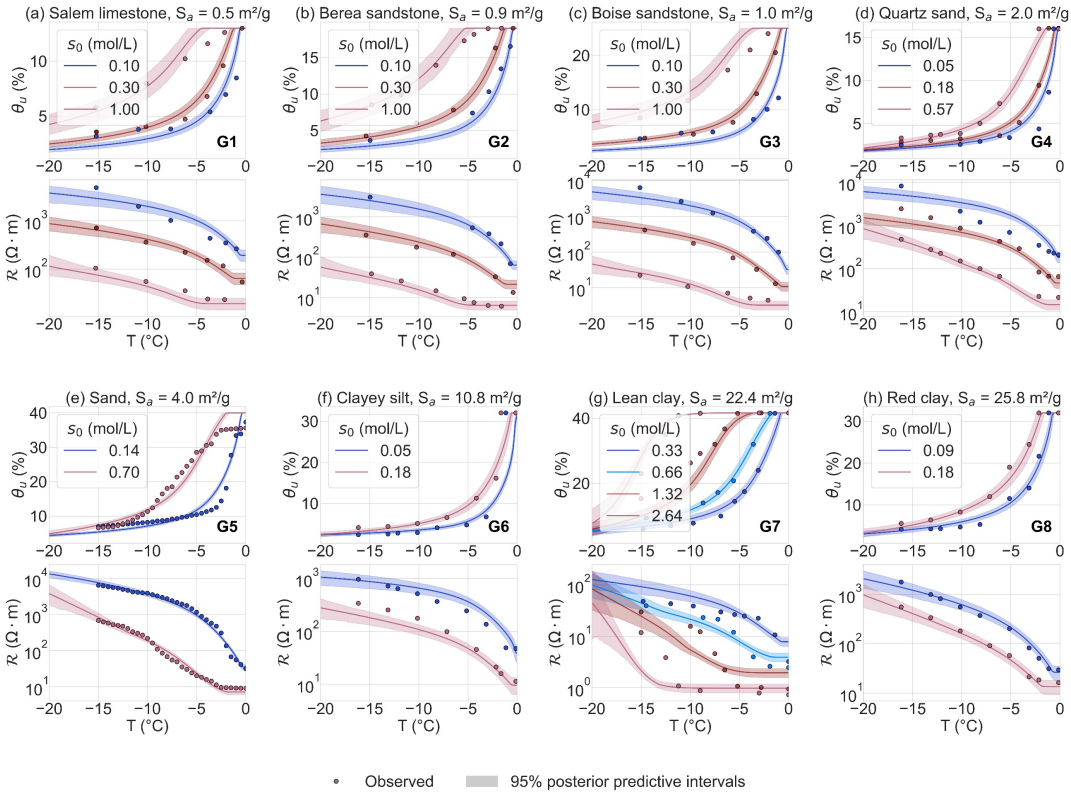


FIGURE 3. Permafrost attribute model calibration for Salem limestone, Berea sandstone, Boise sandstone (Pandit and King 1979), Quartz sand, Clayey silt, Red clay (Luo et al. 2024), Sand (Tang et al., 2020), Lean clay (Liu et al. 2020). The upper panel for each group compares observed and modeled volumetric unfrozen water content, θ_{uw}, and the lower panel compares observed and modeled $\mathcal{R}$. Points are laboratory observations, solid lines are posterior medians, and shaded bands are 95% posterior predictive intervals. Colors denote different initial salinity s_0.

The Bayesian calibration is implemented in Python using CmdStanPy (Stan Development Team, 2024). The prior distributions assigned to the global mean parameters $\boldsymbol{\alpha}_\mathbf{m}$ are summarized in Table 1. Additional details of the statistical model are provided in **Text S3** in the **Supporting**

Information. The posterior distributions of $\boldsymbol{\alpha}_{\mathbf{m}}$ and $\boldsymbol{\alpha}_{\mathbf{d},c}$ are shown in **Figure S1** and **Figure S2 of Supporting Information,** respectively.

TABLE 1. Summary of prior and posterior distributions of $\boldsymbol{\alpha}_{\mathbf{m}}$

Variables	Prior distributions	Descriptions	Posterior distributions		
			Mean	5% value	95% value
ER model					
$\log_{10} k_{s,m}$	$N(-9, 1)$	Prior knowledge of Archie's parameters	-11.3420	-12.8353	-10.1641
m_m	$N(3, 1)$	suggests the informative priors (Glover	3.0612	2.6711	3.4644
n_m	$N(3, 1)$	2016, Herring et al. 2019)	2.8717	2.5590	3.2050
UWC model					
$\alpha_{0,m}$	$N(0.06, 0.1)$	Assume tightening bounds and informative	0.1905	0.1149	0.2586
$\alpha_{1,m}$	$N(0.13, 0.1)$	priors based on deterministic modeling	0.8002	0.4918	1.1940
$\alpha_{2,m}$	$N(-0.2, 0.1)$	result in Figure B1	-0.1421	-0.2259	-0.0769

* N represents normal distribution.

4.2. Sensitivity analysis

Using the same database $\mathbf{D}_{lab}$ and posterior ensemble described above, SHAP analysis is used to quantify the relative influence of soil properties and calibrated model parameters on the coupled forward predictions. The analysis considers ten explanatory variables, including T, s_0, S_a, θ_s, the three UWC model parameters (α_0, α_1, α_2), and the three EC model parameters (m, n, K_s). The model outputs are θ_{uw}, θ_i, and $\log_{10}\mathcal{R}$. Mean absolute SHAP values are used as the importance metric, with larger values indicating stronger average influence on a given output (Lundberg and Lee 2017).

The sensitivity of θ_{uw} is dominated by T, followed by s_0 and S_a (Figure 4a). This ordering agrees with the UWC formulation, in which temperature controls freezing, salinity determines freezing-point depression, and specific surface area governs interfacial and adsorbed water retention. For θ_i, the dominant controls are θ_s and T, followed by s_0 and S_a (Figure 4b). The strong contribution of θ_s reflects the phase-volume constraint, while the effects of T, s_0, and S_a arise through their control of θ_{uw}. The sensitivity of $\log_{10}\mathcal{R}$ is dominated by s_0, followed by T, S_a, m, θ_s, and n (Figure 4c). Salinity affects resistivity through both pore solution conductivity and freezing-point depression, whereas T and S_a regulate the amount and distribution of unfrozen water. The contributions of m and n reflect the dependence of electrical conduction on pore structure and liquid saturation. These rankings are specific to the parameter ranges and correlations represented in the laboratory dataset.

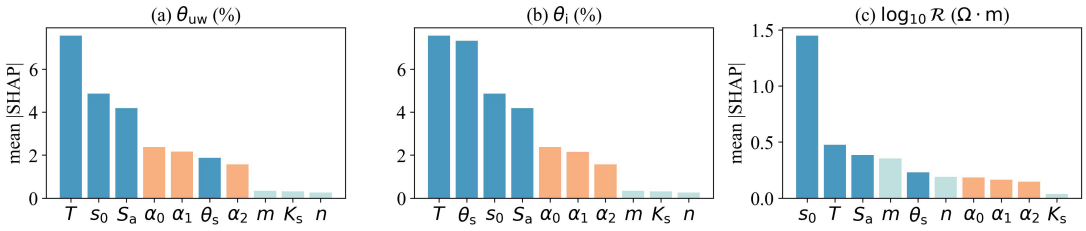


FIGURE 4. Mean absolute SHAP values for model inputs controlling θ_{uw}, θ_i, and $\mathcal{R}$

5. Site-specific investigation

The hierarchical Bayesian inversion framework was applied to a site-specific investigation in the coastal tundra near Utqiaġvik, Alaska (Figure 5a). The region is underlain by continuous, ice-rich permafrost and exhibits pronounced spatial heterogeneity in salinity (Hinkel et al. 2001). The saline conditions primarily reflect marine sediment deposition during past transgressions, followed by freshwater leaching and brine redistribution before and during permafrost formation (Brown 1969, Brigham-Grette and Carter 1992). This depositional and thermal history produced subsurface conditions ranging from nearly fresh ice wedges to moderately saline permafrost and hypersaline cryopegs (Brown 1969, Colangelo-Lillis et al. 2016, Iwahana et al. 2021, Jones et al. 2023).

The two study sites are associated with the NSF Signals in the Soils (SITS) and Next-Generation Ecosystem Experiments Arctic (NGEE Arctic) projects, with boreholes BH#1 and BH#2 located at the SITS and NGEE sites, respectively (Figure 5). Geophysical and meteorological observations were used to construct ERT-inverted resistivity profiles $\mathcal{R}_{\mathbf{pf}}$ and reconstruct ground-temperature profiles $\mathbf{T}_{pf}$. Permafrost attributes and soil freezing characteristic measurements reported by Wang et al. (2026) at five borehole depths were assembled as $\mathbf{D_{bh}}$ and used to update $p_{lab}(\boldsymbol{\alpha})$, yielding the site-conditioned parameter distribution $p_{site}(\boldsymbol{\alpha})$ shown in **Figure S3** of **Supporting Information**. This distribution was adopted as the model parameter prior for both site inversions. The hierarchical Bayesian inversion was then applied independently to BH#1 and BH#2 using weakly informative and borehole measurement-informed priors of $p_0(\mathbf{A})$. The resulting posterior attribute profiles were evaluated against the available borehole observations.

5.1. Geophysical and meteorological data

5.1.1. SITS site

Borehole BH#1 is located within a flat-centered polygon shown in Figure 5b. A 1D resistivity profile was extracted from a 2D ERT transect surveyed on 13 September 2022 (Figure 6a).

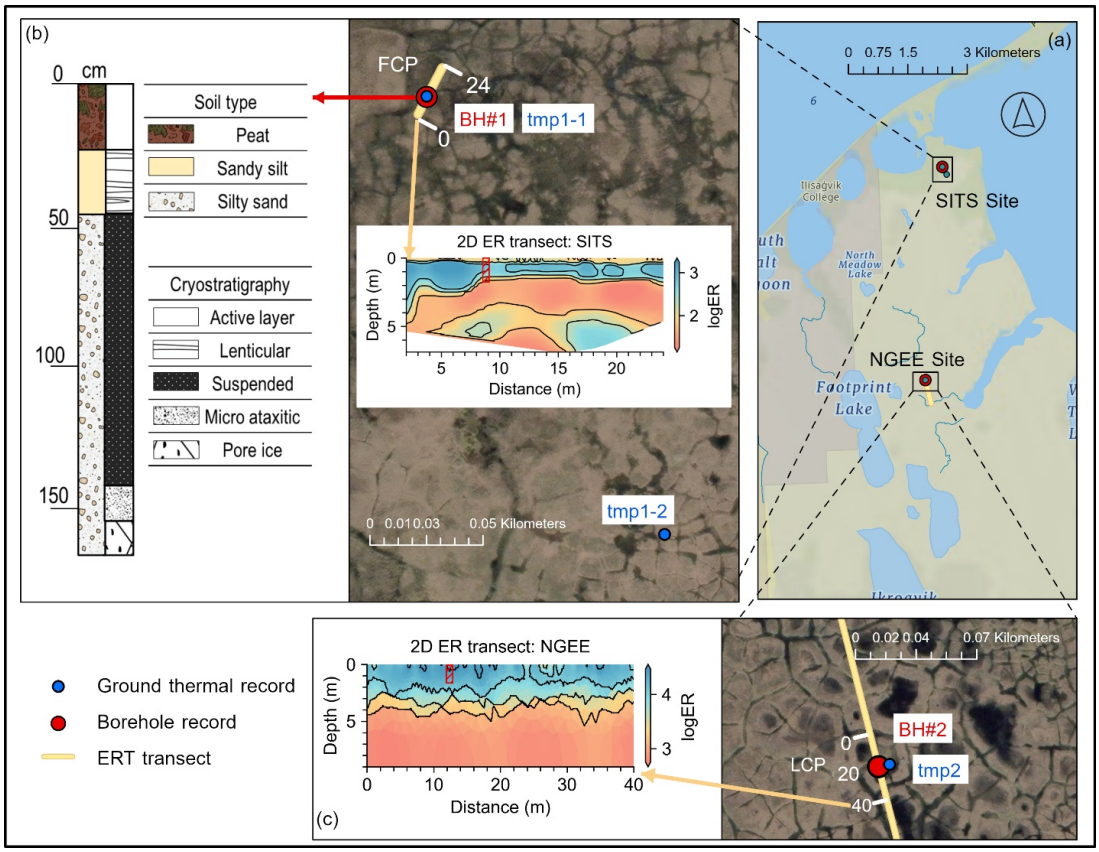


FIGURE 5. Overview of the study sites in Utqiaġvik, Alaska, showing the microtopography, ERT survey lines, and locations of thermal and drilling boreholes. (a) Regional map of geophysical survey locations. (b) The map of BH#1, 2D ERT transect (Tourei et al. 2024), and thermal monitoring locations (tmp1-1, tmp1-2) from SITS project, located in a flat-centered polygon (FCP) area. (c) The map of BH#2, 2D ERT transect (Dafflon et al. 2016), and thermal monitoring location (tmp2) from the NGEE, located in a low-centered polygon (LCP) area.

The ERT data were acquired using combined Wenner–Schlumberger and dipole–dipole arrays with a roll-along configuration. Apparent resistivity measurements were inverted in Res2DInv using smoothness-constrained least squares, a horizontal mesh spacing of 0.25 m, and an initial half-space resistivity of 10 $\Omega \cdot m$. The final inversion had a root-mean-square error of 1.86%.

The ground temperature profile on 13 September 2022 was reconstructed using the 1D Bayesian heat transfer model of Groenke et al. (2023). The model was calibrated using temperature records from sensors at depths of 0.15 and 1.5 m at BH#1, together with records from temperature borehole location tmp1-2 (depth of 0.5 m) located approximately 200 m away

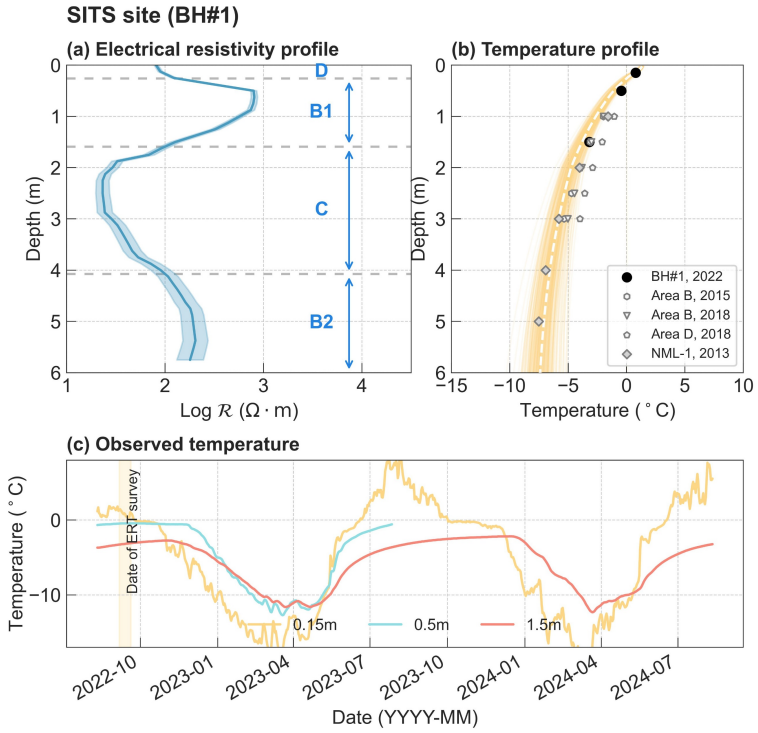


FIGURE 6. 1D electrical resistivity and ground-temperature profiles near SITS site (BH#1), Utqiaġvik, Alaska. Blue shading denotes the 95% uncertainty interval of the inverted resistivity; faint yellow lines and the dashed white line show individual temperature realizations and their ensemble median. Symbols denote borehole measurements, and vertical shaded bars indicate the ERT survey dates.

(Figure 6c). The reconstructed temperature distribution and its posterior uncertainty are shown in Figure 6b. Additional borehole records collected on 13 September 2015 and 2018 at the NGEE Arctic Area B and Area D sites (Romanovsky et al. 2017) and on 13 September 2013 at the nearby NML-1 permafrost monitoring borehole (GTN-P 2015) in the Utqiaġvik, Alaska, region were used to assess the reconstructed temperatures at greater depths.

Undisturbed permafrost cores were collected from the upper approximately 1.7 m on 8 September 2022, preserved under frozen conditions, and characterized for cryostratigraphy, soil freezing characteristics, porosity, salinity, total water content, and other physical properties (Wang et al. 2026).

5.1.2. NGEE Site

Borehole BH#2 is located within a low-centered polygon shown in Figure 5c. The resistivity field was derived from an ERT survey conducted on 28 April 2013 and shown in Figure 7a

(Dafflon et al. 2016). Measurements were collected along an approximately 500-m transect using a dipole–dipole array, 0.5-m electrode spacing, and a roll-along configuration. After data filtering and RTK-GPS position correction, the measurements were inverted in CRTomo using a smoothness-constrained finite-element method. The resulting model had a mean absolute data-model misfit of approximately 10% (Dafflon et al. 2016).

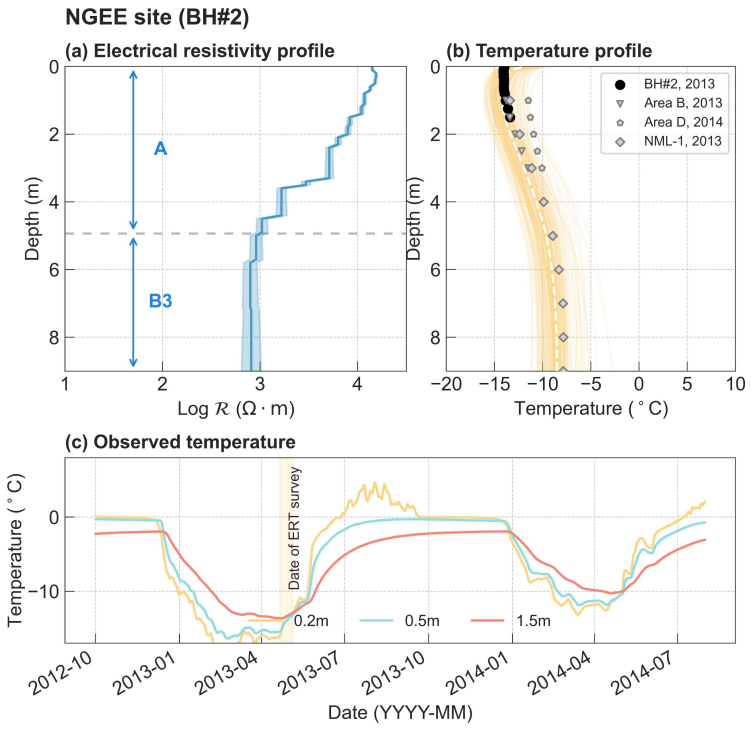


FIGURE 7. Site-specific 1D electrical resistivity and ground temperature profiles near NGEE site (BH#2), Utqiaġvik, Alaska.

The ground temperature profile corresponding to the ERT survey was reconstructed to a depth of 9 m using the Bayesian heat transfer model of Groenke et al. (2023). The borehole record is from September 2012 to September 2023 and contains measurements at 16 depths down to 1.5 m. The reconstructed and measured temperature profiles are compared in Figure 7b. Borehole temperatures collected on 28 April in 2013 and 2014 at the NGEE Arctic Area B, Area D (Romanovsky et al. 2017), and NML-1 permafrost monitoring borehole (GTN-P 2015) in the Utqiaġvik, Alaska, region were used to evaluate the reconstruction at greater depths.

Borehole BH#2 corresponds to core AB#446 in Dafflon et al. (2016), which was recovered along the AB transect using a 5.08 *cm*-diameter soil corer, preserved frozen, and analyzed using

CT imaging and laboratory measurements of bulk density, ice content, organic matter content, and pore water electrical conductivity.

5.2. Evaluation of inversion performance and prior sensitivity

Permafrost attribute profiles along BH#1 and BH#2 are inferred from the 1D electrical resistivity and temperature profiles (Figure 6 and Figure 7), following the workflow illustrated in Figure 2. The resulting posterior attribute profiles are shown in Figure 8 and Figure 9, respectively, and are compared with the available borehole observations. For descriptive interpretation, the 1D profiles are divided into Zones A, B, C, and D as descriptive depth intervals. Zone D corresponds to the active layer where temperatures are above 0°C; as this is outside the scope of physical framework, it is excluded from this analysis. Zones A, B, and C are characterized by electrical resistivity values of approximately 1000–10,000, 100–1000, and 0–100 $\Omega \bullet m$, respectively. Specifically, Zones B1 and B2 of BH#1 and Zone B3 of BH#2 are corresponding to the profile sections with the mean electrical resistivity values of 496, 171 and 825 $\Omega \bullet m$, respectively.

Permafrost attribute profiles at BH#1 and BH#2 were inferred using both weakly informative and borehole-informed θ_s priors. In the weakly informative inversions, the prior distribution for θ_s was centered at 0.40 $m^3\, m^{-3}$, with a standard deviation of 0.125 $m^3\, m^{-3}$. In the borehole-informed inversions, the prior mean was defined by the corresponding core measurements, with a reduced standard deviation of 0.025 $m^3\, m^{-3}$ over the sampled depth intervals.

At BH#1 (Figure 8), the borehole-informed inversion the RMSE of θ_s decreased from 0.1000 to 0.0238 $m^3\, m^{-3}$. Here, the RMSE was calculated as the square root of the mean squared difference between the posterior mean prediction and the corresponding borehole observation at the matched depth. Through the phase volume constraint, the additional information on θ_s also improved the inferred ice-water-solid partitioning. The RMSE of θ_i decreased from 0.1056 to 0.0217 $m^3\, m^{-3}$, and that of θ_{uw} decreased from 0.0255 to 0.0126 $m^3\, m^{-3}$. The changes in s_0 and S_a were comparatively limited, with the s_0 RMSE increasing from 0.0324 to 0.0445 $mol\, L^{-1}$ and the S_a RMSE decreasing from 3.980 to 3.415 $m^2\, g^{-1}$. This contrast is consistent with the structure of the coupled model. The electrical and freezing responses are sensitive to s_0, S_a, and θ_{uw}, which are already constrained by the resistivity and temperature values, whereas θ_s and θ_i are less directly distinguishable from the geophysical observations. The additional θ_s information therefore reduces nonuniqueness in solid-ice partitioning.

At BH#2 (Figure 9), the borehole measurements show pronounced local variability in θ_s within the upper approximately 2 m. The weakly informative inversion captures the overall decrease in θ_s with depth but produces a substantially smoother profile. This smoothing may reflect

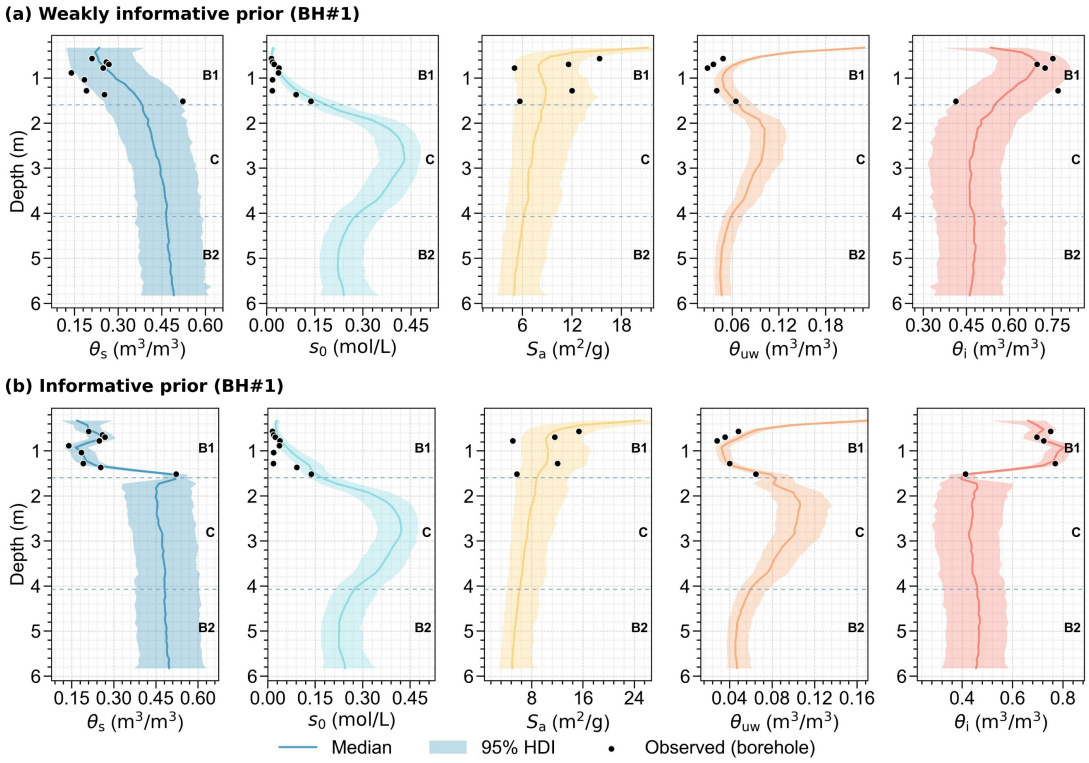


FIGURE 8. Posterior depth profiles of permafrost attributes along BH#1 (SITS site) (a) without borehole-informed priors and (b) with a borehole-informed prior on θ_s at the borehole sampling depths. Solid curves indicate posterior medians, shaded regions indicate 95% highest-density intervals (HDI), and black dots indicate borehole measurements.

the regularization applied during ERT inversion, because the inverted resistivity profile does not resolve corresponding small-scale anomalies over the same depth interval. It may also be attributable to the limited sensitivity of bulk resistivity to the partitioning between mineral solids and ice, neither of which contributes substantially to electrical conduction. When the borehole θ_s measurements are incorporated as prior information, through the phase-volume constraint, the additional information also produces more localized variations in θ_i, θ_{uw}, s_0, and S_a. However, the shallow s_0 RMSE changes only from 0.00234 to 0.00274 $mol\,L^{-1}$.

Overall, imposing direct constraints on θ_s produces substantial changes in the inferred θ_s and θ_i profiles, demonstrating strong coupling between the solid and ice fractions through the phase-volume relationship. By contrast, the estimation errors and broad depth trends of s_0, θ_{uw}, and S_a change only modestly. This response indicates that s_0, θ_{uw}, and S_a attributes are comparatively well constrained by their direct influence on the coupled freezing and electrical

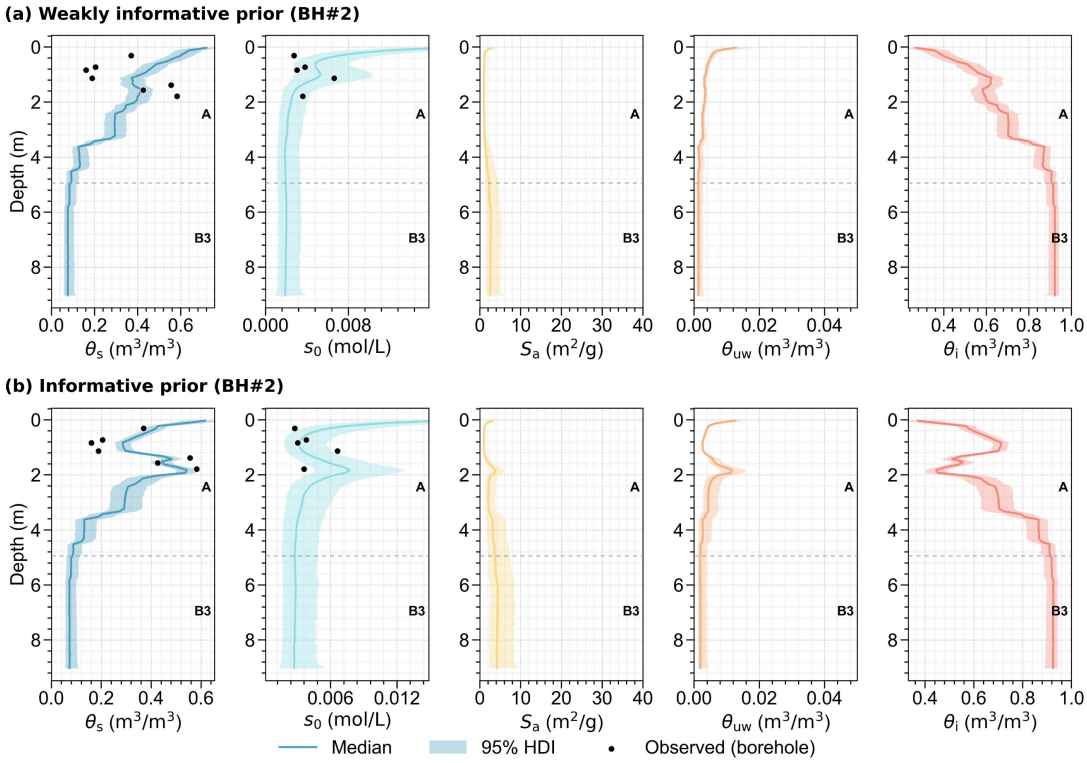


FIGURE 9. Posterior depth profiles of permafrost attributes along BH#2 (NGEE site) with a borehole-informed prior on θ_s at the borehole sampling depths. Solid curves indicate posterior medians, shaded regions indicate 95% highest-density intervals (HDI), and black dots indicate borehole measurements.

conduction behavior, whereas the principal residual non-uniqueness lies in the partitioning between mineral solids and ice.

5.3. Interpretation of inferred permafrost conditions

(1) Upper-permafrost variability near the thaw front: Zones A and B1

Zone B1 at BH#1 and the upper part of Zone A at BH#2 represent shallow permafrost influenced by the seasonal propagation of the surface thermal fluctuation. The temperature records show that annual temperature variations are the largest near the ground surface and progressively attenuate with depth.

The inferred distributions of θ_i indicate locally high ice content at approximately 0.2–1 m depth at both boreholes. This depth corresponds to the transition between the seasonally affected near-surface layer and thermally stable permafrost (Aga et al. 2023), suggesting that the inferred ice-rich layers are associated with repeated freezing and ice segregation near the

long-term thaw front. At BH#1, this interpretation is supported by the lenticular cryostructure observed in the core at depths of 0.25–0.45 m (Wang et al. 2026).

The inferred shallow salinity profiles exhibit contrasting depth-dependent trends at BH#1 and BH#2. At BH1, s_0 increases with depth beneath the near-surface layer. Because the ERT survey was conducted near the end of the thaw season, this pattern may reflect downward solute transport associated with meltwater infiltration through the seasonally thawed layer. At BH#2, inferred s_0 decreases from the ground surface to approximately 1 m and then increases between approximately 1 and 2 m. This pattern is physically plausible for the freezing season, when salt rejection from the advancing freezing front concentrates dissolved ions in the remaining unfrozen pore water below the front.

The inferred decrease in S_a with depth through Zone B1 may indicate a transition from organic, fine-grained near-surface soil to coarser, more mineral-dominated sediment, because higher organic carbon and fine-particle contents are generally associated with larger soil specific surface areas (Arthur et al. 2023).

(2) Deep permafrost conditions below 4–5 m: Zones B2 and B3

Zones B2 at BH#1 and B3 at BH#2 represent the deeper, thermally stable layers of the two profiles. In Zone B2, s_0 is inferred as approximately 0.2 $mol\,L^{-1}$, while θ_{uw} remains near 0.04–0.05 $m^3\,m^{-3}$ and θ_i is approximately 0.45–0.50 $m^3\,m^{-3}$. The persistence of saline unfrozen water therefore provides a physical explanation for the comparatively conductive response (a mean value of 171 $\Omega\,m$) under cold conditions (-8 to $-6\,^{\circ}C$). The inferred moderately ice-rich condition is consistent with the shear-wave velocities of approximately 1100–1600 $m\,s^{-1}$ reported by Tourei et al. (2024).

By contrast, Zone B3 at BH#2 is characterized by low salinity, negligible unfrozen water content, and progressively increasing ice content with depth. The inferred θ_i rises from approximately 0.65–0.70 $m^3\,m^{-3}$ in Zone A to 0.90 $m^3\,m^{-3}$ in Zone B3. These conditions are consistent with the substantially higher resistivity of the BH#2 profile and may indicate the presence of ice-wedge or other massive-ice structures within low-salinity permafrost.

(3) Saline unfrozen conditions in Zone C

Zone C at BH#1 is characterized by electrical resistivity as low as approximately 10–20 $\Omega\,m$ despite persistently subzero ground temperatures. The inferred profiles indicate that this conductive response is associated with elevated s_0 and θ_{uw}. These conditions are consistent with strong freezing point depression and support the presence of saline unfrozen pore water and cryopeg-like conditions.

5.4. Discussion and limitations

The transfer of laboratory-calibrated model parameters to field conditions requires consideration of differences between the laboratory materials and the in-situ soils. For instance, organic soils and highly ice-rich permafrost (θ_i approaching 0.9 $m^3\,m^{-3}$) remain underrepresented in the laboratory calibration database. Such differences may lead to shifts in the model-parameter distributions when the laboratory calibration is applied to in-situ permafrost. This issue was addressed through sequential Bayesian model parameter updating. $p_{lab}(\boldsymbol{\alpha})$ was used as the prior distribution and conditioned with borehole observations to obtain the site-specific distribution $p_{site}(\boldsymbol{\alpha})$. As shown in **Figure S3** of the **Supporting Information**, the two distributions retain substantial overlap for most parameters, with only a moderate shift in α_0 and the site-specific distributions of m, n, and $\log_{10}K_s$ are markedly narrower.

Several limitations should be considered when interpreting the inferred permafrost attributes. First, the site-specific inversion assumes a negligible air fraction. In unsaturated soil, the presence of air reduces liquid-phase connectivity and increases bulk resistivity, this may cause the inversion to attribute part of the electrical response to lower θ_{uw} or higher θ_i and θ_s.

The ERT and petrophysical inversions are treated sequentially. Apparent resistivity data are first inverted to obtain an ERT resistivity model, which is then used as input to the Bayesian petrophysical inversion. Although uncertainty in the ERT-inverted resistivity is included, regularization smoothing, nonlinear inversion effects, and spatially correlated errors are not represented explicitly. Consequently, localized resistivity contrasts and stratigraphic variability may be suppressed, as observed in the upper approximately 2 m at BH#2. Future work could couple the forward modeling of apparent resistivity directly with the petrophysical model. The posterior estimates also remain sensitive to prior specification when the available observations provide weak constraints. Comparison of weakly informative and borehole-informed priors indicates that broad depth trends are relatively stable, whereas localized solid-ice partitioning is more prior dependent.

Finally, the present field application is limited to 1D posterior depth profiles extracted from the ERT-inverted resistivity models and does not estimate a 2D spatial posterior field. Extension to 2D or 3D inversion would require spatially distributed temperature fields. Future developments could combine multidimensional thermal modeling with borehole observations, remote sensing products, and other spatially distributed thermal constraints.

6. Conclusions

This study develops a hierarchical Bayesian inversion framework to infer key physical attributes of saline permafrost from electrical resistivity and temperature observations. Under limited in-situ geophysical observations, the framework combines petrophysical theory, compiled laboratory measurements, and prior knowledge to estimate physically plausible posterior distributions of site-specific permafrost attributes. Within this framework, a physically constrained forward model links temperature, salinity, specific surface area, volumetric solid fraction, volumetric unfrozen water content, and volumetric ice content to ice-water phase partitioning and bulk electrical resistivity. The Bayesian formulation explicitly accounts for uncertainty in laboratory-calibrated parameters, site-specific prior information, and field-scale geophysical measurements. By propagating these uncertainties through the coupled forward model, the approach yields posterior distributions of permafrost attributes rather than single deterministic estimates. Sensitivity analysis identifies temperature, salinity, and specific surface area as the dominant controls on ice-water partitioning, with salinity exerting the strongest influence on electrical resistivity.

Application of the field inversion to two Arctic tundra sites near Utqiaġvik, Alaska demonstrates the model's ability to resolve vertical variations in inferred permafrost conditions, including transitions among ice-rich permafrost, saline partially unfrozen zones, and layers interpreted as massive ice or cryopeg-like conditions. Borehole observations are generally consistent with the posterior estimates, whereas deeper interpretations remain less directly constrained because of limited ground truth data.

The field inversions indicate that non-uniqueness primarily arises from coupling between solid and ice phase partitioning, which limits the independent resolution of volumetric solid and ice fractions. In comparison, salinity, volumetric unfrozen water content, and specific surface area are more directly linked to the coupled temperature-resistivity response. As a result, estimates of volumetric solid and ice fractions are more dependent on physically reasonable prior information, including laboratory measurements, borehole observations, and physically based parameter bounds. The ERT-derived resistivity fields are obtained using regularized inversion, which imposes spatial smoothing and reduces the resolution of fine-scale heterogeneity. Because this inversion step is treated deterministically in the present framework, its associated resolution loss is not explicitly propagated through the Bayesian inversion and may contribute to uncertainty in the inferred permafrost property profiles.

Future advances would benefit from expanded laboratory and field datasets that better constrain the coupled electrical conduction and ice water phase-partitioning behavior of ice-rich and organic-rich soils. Such datasets would improve parameter identifiability, reduce dependence on

prior assumptions, and extend the applicability of Bayesian inversion across a broader range of permafrost conditions.

Acknowledgments

This study is supported by the National Science Foundation under Grants CMMI-2034363, CMMI-2034380, ICER-1927718, ICER-1927708.

Data statement

The compiled laboratory database used for global calibration, the one-dimensional electrical resistivity tomography profile from the SITS site, and the reconstructed ground temperature profile are openly available in the project data repository at `https://github.com/xuey61/saline-permafrost-bayesian-inference-open-data`. The NGEE-Arctic electrical resistivity tomography data were obtained from the ESS-DIVE data portals (Dafflon et al. 2025): `https://data.ess-dive.lbl.gov/datasets/doi:10.5440/1233229`.

References

Aga, J., Boike, J., Langer, M., Ingeman-Nielsen, T., and Westermann, S. 2023. Simulating ice segregation and thaw consolidation in permafrost environments with the CryoGrid community model. The Cryosphere, **17**(10): 4179–4206. Copernicus GmbH. doi:10.5194/tc-17-4179-2023.

Alsharari, B., Olenko, A., and Abuel-Naga, H. 2020. Modeling of electrical resistivity of soil based on geotechnical properties. Expert Systems with Applications, **141**: 112966. doi:10.1016/j.eswa.2019.112966.

Amankwah, S.K., Ireson, A.M., Maulé, C., Brannen, R., and Mathias, S.A. 2021. A model for the soil freezing characteristic curve that represents the dominant role of salt exclusion. Water Resources Research, **57**(8): e2021WR030070. doi:10.1029/2021WR030070.

Anderson, D.M., and Tice, A.R. 1973. The unfrozen interfacial phase in frozen soil water systems. *In* Physical Aspects of Soil Water and Salts in Ecosystems. *Edited by* A. Hadas, D. Swartzendruber, P.E. Rijtema, M. Fuchs, and B. Yaron. Springer, Berlin, Heidelberg. pp. 107–124.

Angelopoulos, M., Overduin, P.P., Jenrich, M., Nitze, I., Günther, F., Strauss, J., Westermann, S., Schirrmeister, L., Kholodov, A., Krautblatter, M., Grigoriev, M.N., and Grosse, G. 2021. Onshore Thermokarst Primes Subsea Permafrost Degradation. Geophysical Research Letters, **48**(20): e2021GL093881. doi:10.1029/2021GL093881.

Archie, G.E. 1942. The Electrical Resistivity Log as an Aid in Determining Some Reservoir Characteristics. Transactions of the AIME, **146**(01): 54–62. doi:10.2118/942054-G.

Arthur, E., Tuller, M., Norgaard, T., Moldrup, P., Chen, C., Ur Rehman, H., Weber, P.L., Knadel, M., and Wollesen de Jonge, L. 2023. Contribution of organic carbon to the total specific surface area of soils with varying clay mineralogy. Geoderma, **430**: 116314. doi:10.1016/j.geoderma.2022.116314.

Banin, A., and Anderson, D.M. 1974. Effects of Salt Concentration Changes During Freezing on the Unfrozen Water Content of Porous Materials. Water Resources Research, **10**(1): 124–128. doi:10.1029/WR010i001p00124.

Bozorgzadeh, N., Harrison, J.P., and Escobar, M.D. 2019. Hierarchical Bayesian modelling of geotechnical data: application to rock strength. Géotechnique, **69**(12): 1056–1070. doi:10.1680/jgeot.17.P.282.

Brigham-Grette, J., and Carter, L.D. 1992. Pliocene Marine Transgressions of Northern Alaska: Circumarctic Correlations and Paleoclimatic Interpretations. ARCTIC, **45**(1): 74–89. doi:10.14430/arctic1375.

Brown, J. 1969. Ionic Concentration Gradients in Permafrost, Barrow, Alaska. Corps of Engineers, U.S. Army, Cold Regions Research and Engineering Laboratory.

Bublik, S., Semin, M., Levin, L., Brovka, A., and Dedyulya, I. 2023. Experimental and Theoretical Study of the Influence of Saline Soils on Frozen Wall Formation. Applied Sciences, **13**(18): 10016. Multidisciplinary Digital Publishing Institute. doi:10.3390/app131810016.

Chen, Y., Zhou, Z., Wang, J., Zhao, Y., and Dou, Z. 2021. Quantification and division of unfrozen water content during the freezing process and the influence of soil properties by low-field nuclear magnetic resonance. Journal of Hydrology, **602**: 126719. doi:10.1016/j.jhydrol.2021.126719.

Colangelo-Lillis, J., Eicken, H., Carpenter, S.D., and Deming, J.W. 2016. Evidence for marine origin and microbial-viral habitability of sub-zero hypersaline aqueous inclusions within permafrost near Barrow, Alaska. FEMS microbiology ecology, **92**(5): fiw053. doi:10.1093/femsec/fiw053.

Dafflon, B., Hubbard, S., Peterson, J., and Ulrich, C. 2025. Electrical resistivity tomography, electromagnetic data, and permafrost cores acquired near Utqiagvik, Alaska, 2011-2015. Next-Generation Ecosystem Experiments (NGEE) Arctic, ESS-DIVE repository.

Dafflon, B., Hubbard, S., Ulrich, C., Peterson, J., Wu, Y., Wainwright, H., and Kneafsey, T.J. 2016. Geophysical estimation of shallow permafrost distribution and properties in an ice-wedge polygon-dominated Arctic tundra region. GEOPHYSICS, **81**(1): WA247–WA263. Society of Exploration Geophysicists. doi:10.1190/geo2015-0175.1.

Dall'Amico, M., Endrizzi, S., Gruber, S., and Rigon, R. 2011. A robust and energy-conserving model of freezing variably-saturated soil. The Cryosphere, **5**(2): 469–484. Copernicus GmbH. doi:10.5194/tc-5-469-2011.

Dou, S., Nakagawa, S., Dreger, D., and Ajo-Franklin, J. 2016. A rock-physics investigation of unconsolidated saline permafrost: P-wave properties from laboratory ultrasonic measurements. GEOPHYSICS, **81**(1): WA233–WA245. doi:10.1190/geo2015-0176.1.

Fortier, R., LeBlanc, A.-M., Allard, M., Buteau, S., and Calmels, F. 2008. Internal structure and conditions of permafrost mounds at Umiujaq in Nunavik, Canada, inferred from field investigation and electrical resistivity tomography. Canadian Journal of Earth Sciences, **45**(3): 367–387. NRC Research Press. doi:10.1139/E08-004.

Friedman, S.P. 2005. Soil properties influencing apparent electrical conductivity: a review. Computers and Electronics in Agriculture, **46**(1): 45–70. doi:10.1016/j.compag.2004.11.001.

Gao, X., Tian, R., Yin, T., Galindo Torres, S.A., and Lei, L. 2024. Pore-scale freezing of a sandy saline soil visualized with micro- computed tomography. Permafrost and Periglacial Processes, **35**: 1–16. doi:10.1002/ppp.2215.

Gelman, A., Carlin, J.B., Stern, H.S., Dunson, D.B., Vehtari, A., and Rubin, D.B. 2013. Bayesian Data Analysis. *In* 3rd edition. Chapman and Hall/CRC, Boca Raton.

Glover, P.W.J. 2016. Archie's law – a reappraisal. Solid Earth, **7**(4): 1157–1169. Copernicus GmbH. doi:10.5194/se-7-1157-2016.

Groenke, B., Langer, M., Nitzbon, J., Westermann, S., Gallego, G., and Boike, J. 2023. Investigating the thermal state of permafrost with Bayesian inverse modeling of heat transfer. The Cryosphere, **17**(8): 3505–3533. Copernicus GmbH. doi:10.5194/tc-17-3505-2023.

GTN-P. 2015. Global Terrestrial Network for Permafrost metadata for permafrost boreholes (TSP). PANGAEA.

Hauck, C., Böttcher, M., and Maurer, H. 2011. A new model for estimating subsurface ice content based on combined electrical and seismic data sets. The Cryosphere, **5**(2): 453–468. Copernicus GmbH. doi:10.5194/tc-5-453-2011.

Herring, T., Cey, E., and Pidlisecky, A. 2019. Electrical resistivity of a partially saturated porous medium at subzero temperatures. Vadose Zone Journal, **18**(1): 190019. doi:10.2136/vzj2019.02.0019.

Hinkel, K.M., Doolittle, J.A., Bockheim, J.G., Nelson, F.E., Paetzold, R., Kimble, J.M., and Travis, R. 2001. Detection of subsurface permafrost features with ground-penetrating radar, Barrow, Alaska. Permafrost and Periglacial Processes, **12**(2): 179–190. doi:10.1002/ppp.369.

Hjort, J., Streletskiy, D., Doré, G., Wu, Q., Bjella, K., and Luoto, M. 2022. Impacts of permafrost degradation on infrastructure. Nature Reviews Earth & Environment, **3**(1): 24–38. Nature Publishing Group. doi:10.1038/s43017-021-00247-8.

Iwahana, G., Cooper, Z.S., Carpenter, S.D., Deming, J.W., and Eicken, H. 2021. Intra-ice and intra-sediment cryopeg brine occurrence in permafrost near Utqiaġvik (Barrow). Permafrost and Periglacial Processes, **32**(3): 427–446. doi:10.1002/ppp.2101.

Jin, X., Yang, W., Gao, X., Zhao, J.-Q., Li, Z., and Jiang, J. 2020. Modeling the unfrozen water content of frozen soil based on the absorption effects of clay surfaces. Water Resources Research, **56**(12): e2020WR027482. doi:10.1029/2020WR027482.

Jones, B.M., Kanevskiy, M.Z., Parsekian, A.D., Bergstedt, H., Ward Jones, M.K., Rangel, R.C., Hinkel, K.M., and Shur, Y. 2023. Rapid Saline Permafrost Thaw Below a Shallow Thermokarst Lake in Arctic Alaska. Geophysical Research Letters, **50**(22): e2023GL105552. doi:10.1029/2023GL105552.

Kan, R., and Sen, P.N. 1987. Electrolytic conduction in periodic arrays of insulators with charges. The Journal of Chemical Physics, **86**(10): 5748–5756. doi:10.1063/1.452502.

Khabaz, Z.T., Ghanati, R., and Bérubé, C.L. 2024. Uncertainty quantification in electrical resistivity tomography inversion: hybridizing block-wise bootstrapping with geostatistics. Geophysical Journal International, **239**(3): 1576–1596. doi:10.1093/gji/ggae347.

Liu, J., Yang, P., and Yang, Z. (Joey). 2020. Electrical properties of frozen saline clay and their relationship with unfrozen water content. Cold Regions Science and Technology, **178**: 103127. doi:10.1016/j.coldregions.2020.103127.

Lundberg, S.M., and Lee, S.-I. 2017. A unified approach to interpreting model predictions. *In* Proceedings of the 31st International Conference on Neural Information Processing Systems. Curran Associates Inc., Red Hook, NY, USA. pp. 4768–4777.

Luo, H., Jougnot, D., Jost, A., Teng, J., Mendieta, A., Lin, G., and Thanh, L.D. 2024. Predicting the Electrical Conductivity of Partially Saturated Frozen Porous Media, a Fractal Model for Wide Ranges of Temperature and Salinity. Water Resources Research, **60**(3): e2023WR034845. doi:10.1029/2023WR034845.

Mavritsakis, A., Schweckendiek, T., Teixeira, A.M., and Smyrniou, E. 2022. Hierarchical Bayesian modelling for geotechnical parameter derivation. *In* 8th International Symposium on Reliability Engineering and Risk Management. Research Publishing Services. pp. 398–405.

Maxwell, J.C., and Niven, W.D. (William D. 1881. A treatise on electricity and magnetism. Oxford, Clarendon Press.

Mikucki, J.A., Auken, E., Tulaczyk, S., Virginia, R.A., Schamper, C., Sørensen, K.I., Doran, P.T., Dugan, H., and Foley, N. 2015. Deep groundwater and potential subsurface habitats beneath an Antarctic dry valley. Nature Communications, **6**(1): 6831. Nature Publishing Group. doi:10.1038/ncomms7831.

Ming, F., Li, D.Q., and Chen, L. 2020. Electrical Resistivity of Freezing Clay: Experimental Study and Theoretical Model. Journal of Geophysical Research: Earth Surface, **125**(2): e2019JF005267. doi:10.1029/2019JF005267.

Minsley, B.J., Abraham, J.D., Smith, B.D., Cannia, J.C., Voss, C.I., Jorgenson, M.T., Walvoord, M.A., Wylie, B.K., Anderson, L., Ball, L.B., Deszcz-Pan, M., Wellman, T.P., and Ager, T.A. 2012. Airborne electromagnetic imaging of discontinuous permafrost. Geophysical Research Letters, **39**(2). doi:10.1029/2011GL050079.

Mualem, Y., and Friedman, S.P. 1991. Theoretical Prediction of Electrical Conductivity in Saturated and Unsaturated Soil. Water Resources Research, **27**(10): 2771–2777. doi:10.1029/91WR01095.

Muñoz-Sabater, J., Dutra, E., Agustí-Panareda, A., Albergel, C., Arduini, G., Balsamo, G., Boussetta, S., Choulga, M., Harrigan, S., Hersbach, H., Martens, B., Miralles, D.G., Piles, M., Rodríguez-Fernández, N.J., Zsoter, E., Buontempo, C., and Thépaut, J.-N. 2021. ERA5-Land: a state-of-the-art global reanalysis dataset for land applications. Earth System Science Data, **13**(9): 4349–4383. Copernicus GmbH. doi:10.5194/essd-13-4349-2021.

Ostroumov, V., Hoover, R., Ostroumova, N., Van Vliet-Lanoë, B., Siegert, C., and Sorokovikov, V. 2001. Redistribution of soluble components during ice segregation in freezing ground. Cold Regions Science and Technology, **32**(2): 175–182. doi:10.1016/S0165-232X(01)00031-3.

Pandit, B.I., and King, M.S. 1979. A study of the effects of pore-water salinity on some physical properties of sedimentary rocks at permafrost temperatures. Canadian Journal of Earth Sciences, **16**(8): 1566–1580. doi:10.1139/e79-143.

Puga, J.L., Krzywinski, M., and Altman, N. 2015. Bayesian statistics. Nature Methods, **12**(5): 377–378. Nature Publishing Group. doi:10.1038/nmeth.3368.

Revil, A., Cathles, L.M., Losh, S., and Nunn, J.A. 1998. Electrical conductivity in shaly sands with geophysical applications. Journal of Geophysical Research: Solid Earth, **103**(B10): 23925–23936. doi:10.1029/98JB02125.

Revil, A., and Glover, P.W.J. 1997. Theory of ionic-surface electrical conduction in porous media. Physical Review B, **55**(3): 1757–1773. American Physical Society. doi:10.1103/PhysRevB.55.1757.

Revil, A., and Gresse, M. 2021. Induced Polarization as a Tool to Assess Alteration in Geothermal Systems: A Review. Minerals, **11**(9): 962. Multidisciplinary Digital Publishing Institute. doi:10.3390/min11090962.

Rhoades, J.D., Raats, P. a. C., and Prather, R.J. 1976. Effects of Liquid-phase Electrical Conductivity, Water Content, and Surface Conductivity on Bulk Soil Electrical Conductivity. Soil Science Society of America Journal, **40**(5): 651–655. doi:10.2136/sssaj1976.03615995004000050017x.

Romanovsky, V., Nicolsky, D., Wright, T., Cable, W., and Dolgikh, K. 2017. Thermal Conductivity and Heat Flux, Area A, B, C, and D, Utqiagvik (Barrow), Alaska, 2012-2023.

Rossi, M., Dal Cin, M., Picotti, S., Gei, D., Isaev, V.S., Pogorelov, A.V., Gorshkov, E.I., Sergeev, D.O., Kotov, P.I., Giorgi, M., and Rainone, M.L. 2022. Active Layer and Permafrost Investigations Using Geophysical and Geocryological Methods—A Case Study of the Khanovey Area, Near Vorkuta, in the NE European Russian Arctic. Frontiers in Earth Science, **10**.

Sen, P.N., Scala, C., and Cohen, M.H. 1981. A self-similar model for sedimentary rocks with application to the dielectric constant of fused glass beads. Geophysics, **46**(5): 781–795. doi:10.1190/1.1441215.
Shock, E.L., and Boyd, E.S. 2015. Principles of Geobiochemistry. Elements, **11**(6): 395–401. doi:10.2113/gselements.11.6.395.
Shubin, V.E., Hunter, R.J., and O'Brien, R.W. 1993. Electroacoustic and Dielectric Study of Surface Conduction. Journal of Colloid and Interface Science, **159**(1): 174–183. doi:10.1006/jcis.1993.1309.
Shur, Y., Hinkel, K.M., and Nelson, F.E. 2005. The transient layer: implications for geocryology and climate-change science. Permafrost and Periglacial Processes, **16**(1): 5–17. doi:10.1002/ppp.518.
Tang, R., Zhou, G., Wang, J., Zhao, G., Lai, Z., and Jiu, F. 2020. A new method for estimating salt expansion in saturated saline soils during cooling based on electrical conductivity. Cold Regions Science and Technology, **170**: 102943. doi:10.1016/j.coldregions.2019.102943.
Tourei, A., Ji, X., Rocha dos Santos, G., Czarny, R., Rybakov, S., Wang, Z., Hallissey, M., Martin, E.R., Xiao, M., Zhu, T., Nicolsky, D., and Jensen, A. 2024. Mapping permafrost variability and degradation using seismic surface waves, electrical resistivity, and temperature sensing: a case study in Arctic Alaska. Journal of Geophysical Research: Earth Surface, **129**(3): e2023JF007352. doi:10.1029/2023JF007352.
Wagner, F.M., Mollaret, C., Günther, T., Kemna, A., and Hauck, C. 2019. Quantitative imaging of water, ice and air in permafrost systems through petrophysical joint inversion of seismic refraction and electrical resistivity data. Geophysical Journal International, **219**(3): 1866–1875. doi:10.1093/gji/ggz402.
Wang, Y., and Hu, L. 2023. A theoretical model of soil freezing characteristic curve considering the freezing of adsorbed water and capillary water. Water Resources Research, **59**(7): e2023WR034662. doi:10.1029/2023WR034662.
Wang, Z., Xiao, M., Bray, M., Nicolsky, D., and Ji, X. 2026. Creep deformation and long-term strength of ice-rich permafrost in Northern Alaska. Journal of Geotechnical and Geoenvironmental Engineering, **152**(1): 04025161. American Society of Civil Engineers. doi:10.1061/JGGEFK.GTENG-13324.
Waxman, M.H., and Smits, L.J.M. 1968. Electrical Conductivities in Oil-Bearing Shaly Sands. Society of Petroleum Engineers Journal, **8**(02): 107–122. doi:10.2118/1863-A.
Winsauer, W.O., Shearin, H.M., Jr., Masson, P.H., and Williams, M. 1952. Resistivity of Brine-Saturated Sands in Relation to Pore Geometry. AAPG Bulletin, **36**(2): 253–277. doi:10.1306/3D9343F4-16B1-11D7-8645000102C1865D.
Yang, W.-H., Clifford, D., and Minasny, B. 2015. Mapping soil water retention curves via spatial Bayesian hierarchical models. Journal of Hydrology, **524**: 768–779. doi:10.1016/j.jhydrol.2015.03.029.
Zhou, J., Meng, X., Wei, C., and Pei, W. 2020. Unified soil freezing characteristic for variably-saturated saline soils. Water Resources Research, **56**(7): e2019WR026648. doi:10.1029/2019WR026648.

Appendix A. Derivation of the Revil-based electrical conductivity model for saline frozen soil

Following the surface conduction effective medium formulation (Kan and Sen 1987, Shubin et al. 1993) and its application to shaly sands by Revil et al. (1998), the dimensionless parameter ξ is introduced to quantify the relative importance of interfacial conduction compared with pore fluid conduction.

$$\xi = \frac{\sigma_s}{\sigma_f} \tag{A1}$$

where σ_s is the equivalent surface conductivity associated with interfacial counterion transport. ξ is related to the excess surface charge per unit pore volume Q_v as (Revil et al., 1998)

$$\xi = \frac{2}{3}\frac{\phi}{1-\phi}\frac{Z_s \beta_s Q_v}{\sigma_f} \tag{A2}$$

where Z_s is the counterion valence and β_s is the equivalent surface mobility of the counterions. The excess charge concentration Q_v is commonly related to the cation exchange capacity, CEC, by

$$Q_v = \rho_s \frac{1-\phi}{\phi} CEC \tag{A3}$$

where ρ_s is the grain density. In the present study, the specific surface area S_a is used as a proxy for the available mineral-water interfacial area (Revil and Gresse 2021),

$$CEC \approx q_s S_a \tag{A4}$$

where q_s is an effective surface charge density. Substituting Eq. (A4) into Eq. (A3), and then into Eq. (A2), yields

$$\xi = \frac{K_s S_a}{\sigma_f} \tag{A5}$$

with

$$K_s = \frac{2}{3} Z_s \beta_s \rho_s q_s \tag{A6}$$

For a dilute electrolyte solution, σ_f can be expressed as the sum of the contributions from all mobile ionic species (Revil and Glover 1997),

$$\sigma_f = F_A \sum_i Z_i \beta_i^f C_i \tag{A7}$$

where F_A is Faraday's constant, Z_i is the absolute ionic valence of species i, β_i^f is the ionic mobility in the free electrolyte, and C_i is the molar concentration of species i $mol\, m^{-3}$. Assuming NaCl is the dominant pore solute, the fluid conductivity approximates

$$\sigma_f = a_s C = F_A \left(\beta_{Na^+}^f + \beta_{Cl^-}^f \right) C \approx 0.0126\ C = 12.6 s_0 / S_{ru} \tag{A8}$$

where C is the equivalent NaCl concentration, and $C = 10^3 s_0 / S_{ru}$; $a_s = F_A(\beta_{Na^+}^f + \beta_{Cl^-}^f) \approx 0.0126\ S\, m^2\, mol^{-1}$.

Appendix B. Derivation and parameterization of the UWC model

A microscale analysis of the interfacial effects, adsorption force, and ion concentration in freezing soil was presented by Jin et al. (2020). The expression of w_u is given as:

(B1)
$$w_u = (S_a\sqrt{T'})\left[\left(\frac{1}{\alpha}\sqrt{\frac{N}{v^3}}\sqrt{\frac{K_f\varepsilon k}{2\pi e^2}}\times 10^2\right)|T|^{-0.5} + \frac{\alpha-1}{2\alpha v}\sqrt{\frac{\varepsilon k}{2\pi s_0 e^2}}\times 10^2 + \frac{0.05}{\sqrt{T'}}\right], T \le T_w$$

where $T' \approx \sqrt{273+T}$, represents the square root of the absolute temperature (in Kelvin); and the other parameters $(N, \nu, K_f, \varepsilon, \kappa, e, \alpha)$ relate to the physicochemical properties of the salt solution and soil mineral surface. The detailed definitions of these parameters can be found in Jin et al. (2020).

For practical applications, the theoretical model in Eq. (B1) is parameterized and linearized. The expression is simplified into two components, A_1 and A_2, which represent the intercept and slope of the UWC-temperature relationship, respectively:

(B2)
$$\frac{w_u - 0.05S_a}{S_a^\ell\sqrt{273+T}} = A_1|T|^{-0.5} + A_2$$
$$\begin{cases} A_1 = \frac{1}{\alpha}\sqrt{\frac{N}{v^3}}\sqrt{\frac{K_f\varepsilon k}{2\pi e^2}}\times 10^2 \\ A_2 = \frac{\alpha-1}{2\alpha v}\sqrt{\frac{\varepsilon k}{2\pi s_0 e^2}}\times 10^2 \end{cases}$$

In Eq. (B2), N, v, ε, k, and e are presumed as constants. α is found to increase with salt concentration (Jin et al., 2020). K_f expresses the relationship between the freezing temperature and concentration of ionic solution. In summary, the model evaluates UWC by two factors: the specific surface area S_a and salinity s_0, where α and K_f are regarded as functions of s_0.

Figure B1(a) plots the regression lines between normalized temperature ($|T|^{-0.5}$) and normalized UWC ($\frac{w_u-0.05S_a}{S_a^\ell\sqrt{273+T}}$). The effect of S_a is integrated into the normalized unfrozen water content term. The figure demonstrates linear relationships between normalized temperature and unfrozen water content. The color bar represents salinity variations, showing that when salinity increases, the slope (A_1) of these linear relationships increases while the intercept (A_2) decreases. Based on an empirical analysis of UWC and EC dataset (further described in **Text S2** in **Supporting Information**), the parameters A_1 and A_2 were found to exhibit a linear relationship with s_0 (**Figure B1**b–c). These empirical relationships are assumed as:

(B3)
$$A_1 = \alpha_0 + \alpha_1 s_0$$
$$A_2 = \alpha_2 s_0$$

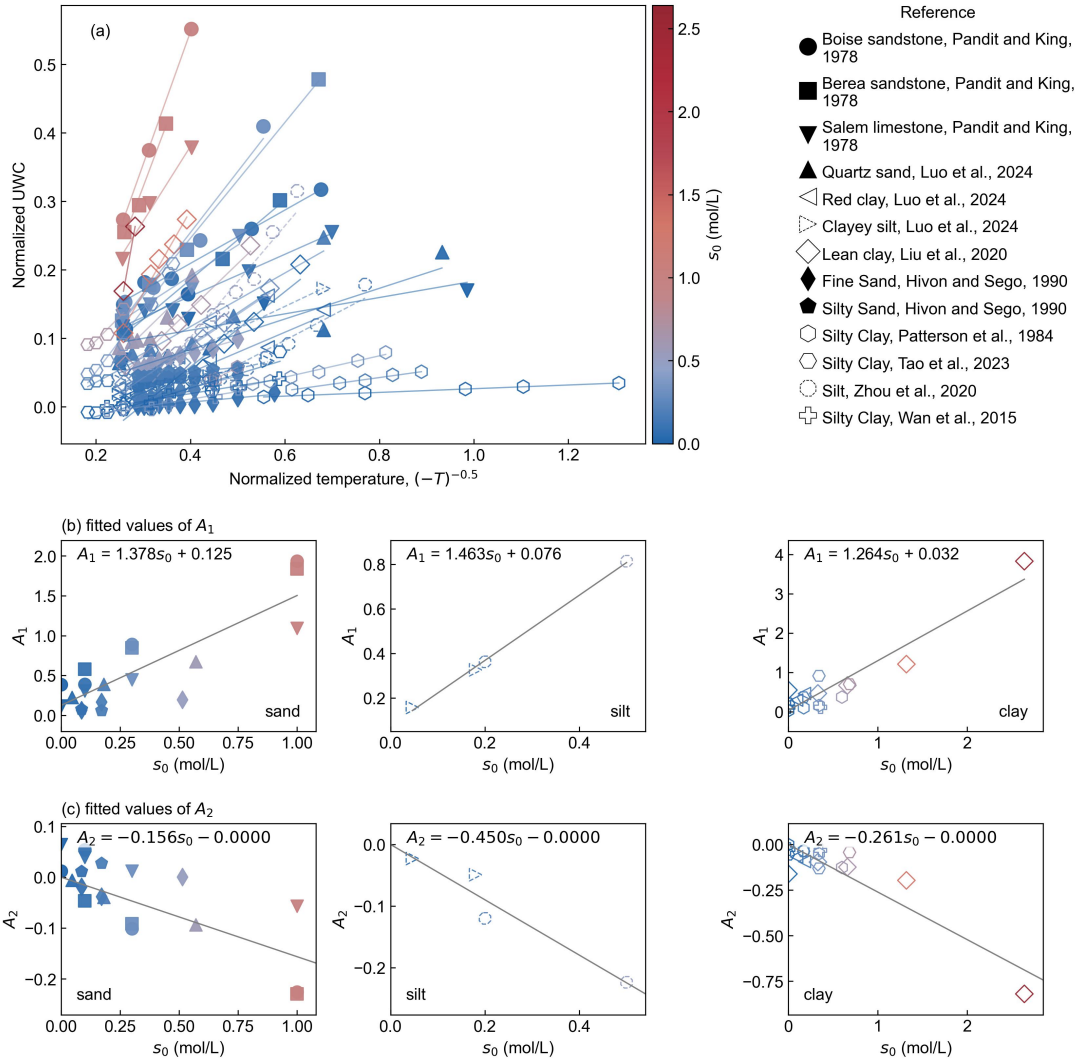


FIGURE B1. Linearization of UWC model: (a) normalized temperature versus normalized unfrozen water content at various salinities. Note that the relationship is observed nearly linear, and the slope and intercept are found to vary with salinity. (b) and (c) the "best-fit" linear relationships between initial salinity with slope (A_1) and intercept (A_2), respectively, of normalized T-UWC regression. (Sand, clay, and silt are represented by markers with “solid fill + solid border”, “hollow + solid border”, and “hollow + dashed border”, respectively)